Applied Catalysis B: Environment and Energy 377 (2025) 125504

Contents lists available at ScienceDirect

Applied Catalysis B: Environment and Energy

journal homepage: www.elsevier.com/locate/apcatb

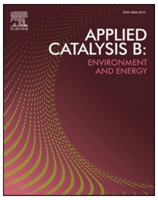

Bio-based piperidines as liquid organic hydrogen (deuterium) carrier over Pd catalysts

Zihang Yin [a,b,1], Sicong Ma [c,1], Yanwei Cao [a,*], Lin Chen [d], Zhi-Pan Liu [c,d], Jing Niu [e], Fangxiu Ye [e,f], Shutao Xu [e,g], Long Pan [b,*], Lin He [a,*]

[a] *State Key Laboratory of Low Carbon Catalysis and Carbon Dioxide Utilization, Lanzhou Institute of Chemical Physics (LICP), Chinese Academy of Sciences, No.18 Tianshui Middle Road, Lanzhou 730000, China*
[b] *Key Laboratory of Advanced Metallic Materials of Jiangsu Province, Southeast University, School of Materials Science and Engineering, Southeast University, 2 Southeast University Road, Nanjing 211189, China*
[c] *State Key Laboratory of Metal Organic Chemistry, Shanghai Institute of Organic Chemistry, Chinese Academy of Sciences, Shanghai 200032, China*
[d] *Collaborative Innovation Center of Chemistry for Energy Material, Shanghai Key Laboratory of Molecular Catalysis and Innovative Materials, Key Laboratory of Computational Physical Science, Department of Chemistry, Fudan University, Shanghai 200433, China*
[e] *National Engineering Research Center of Lower-Carbon Catalysis Technology, Dalian Institute of Chemical Physics, Chinese Academy of Sciences, Dalian 116023, China*
[f] *University of Chinese Academy of Sciences, Beijing 100049, China*
[g] *The State Key Laboratory of Catalysis, Dalian Institute of Chemical Physics, Chinese Academy of Sciences, Dalian 116023, China*

ARTICLE INFO

Keywords:
Liquid organic hydrogen carriers
Bio-based piperidine
Size-dependent
Palladium
Deuterium

ABSTRACT

Bio-based Liquid organic hydrogen carriers (LOHC) present a viable and renewable alternative for hydrogen storage. Herein, we proposed a LOHC system that employs size-controlled Pd nanoparticles as dehydrogenation/hydrogenation catalysts, in combination with bio-based piperidine derivatives as hydrogen carriers. Through precise synthesis, we fabricated Pd/C catalysts with well-defined active sites ranging from single-atom (SA) to nanoclusters (NCs) and nanoparticles (NPs). Pd_{SA}/C exhibit no catalytic activity, while Pd5/C (~1.8 nm) showed significantly higher activity than the Pd1/C (~0.9 nm), despite the latter having a smaller particle size and a larger electrochemically active surface area (ECSA). This finding suggests that smaller is not always better in catalyst design. Comprehensive analyses of catalyst morphology and electronic structure analyses established clear structure-activity relationships between the particle size of Pd species and hydrogen release performance. Furthermore, experimental results and density functional theory (DFT) calculations demonstrated that the position of methyl-substitution strongly impacts dehydrogenation efficiency, with 2-methylpiperidine achieving the highest activity compared to piperidine and its 3-/4-methyl isomers. The application of this LOHC system was extended to deuterium (D) storage, underscoring its potential for broader hydrogen isotope management technologies. This study validates bio-based piperidines as promising, sustainable, and scalable next-generation LOHC platforms.

1. Introduction

Hydrogen (H_2) constitutes a cornerstone of modern industrial systems, serving both as a fundamental raw material in various chemical processes and as a promising energy carrier for future clean energy systems [1,2]. While significant progress has been made in hydrogen production and utilization technologies, hydrogen storage remains a major barrier to fully realizing its potential value [3–6]. Existing storage methods, including high-pressure gas storage, cryogenic liquid hydrogen, and solid-state materials, each have inherent limitations related to safety, efficiency, and cost-effectiveness [7–10]. Given these limitations, Liquid organic hydrogen carriers (LOHC) have gained considerable attention as an alternative solution for hydrogen storage and transportation. By chemically binding hydrogen within stable organic molecules, LOHC enable safer and more efficient transport and release under controlled conditions [11–15]. Among the different LOHC candidates, piperidines has exhibited superior hydrogen storage capacity (HSC, 6.1–7.1 wt%), lower dehydrogenation enthalpy, and the

---

* Corresponding authors.
E-mail addresses: caoyanwei@licp.cas.cn (Y. Cao), panlong@seu.edu.cn (L. Pan), helin@licp.cas.cn (L. He).
[1] These authors contributed equally to this work.

https://doi.org/10.1016/j.apcatb.2025.125504
Received 31 March 2025; Received in revised form 7 May 2025; Accepted 17 May 2025
Available online 18 May 2025

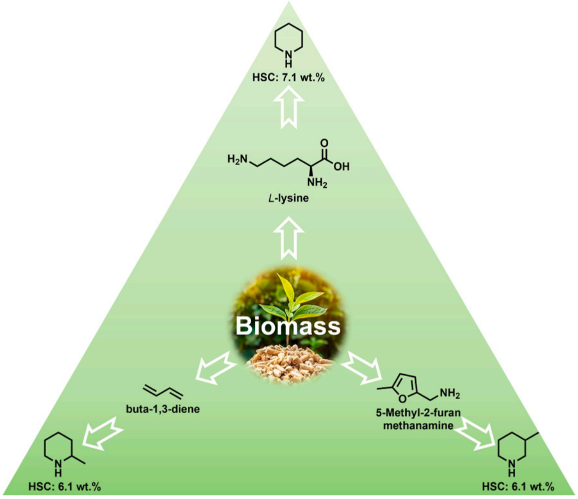

Scheme 1. Synthetic routes to bio-based piperidine derivatives.

absence of undesired by-products during hydrogenation or dehydrogenation cycles [16–19]. Furthermore, piperidines can be synthesized from renewable biomass sources, such as cellulose-derived furan and furfural, bio-based lysine, bio-based butadiene, and methylation of bio-based piperidine [20–22]. In this context, bio-based piperidines offers a sustainable, renewable, and zero-carbon emission approach to hydrogen storage [23,24] (Scheme 1).

Recent advancements in catalytic dehydrogenation of piperidines have significantly enhanced their potential in LOHC applications. Various Pd-based heterogeneous catalysts have been developed for this reaction. For example, Milstein *et al.* reported the dehydrogenation of piperidines using a Pd catalyst [17]. Yamaguchi et al. utilized Pd/LDH for the dehydrogenation of piperidine, achieving yields of 54 % of pyridine at 125°C over 18 h [25]. Voutchkova-Kostal and co-workers employed Pd-doped hydrotalcites for the acceptor-free dehydrogenation of piperidine, achieving yields of 45 % of pyridine at 140°C over 24 h [26]. Despite utilizing the same active component, these studies exhibit significant differences in catalytic performance, highlighting the crucial role of morphology properties and electronic structure in Pd-based catalysts. It is well known that particle size profoundly influences these properties, leading to notable variations in catalytic activity. While the size modulation of metal species has been extensively studied to regulate dehydrogenation performance in systems such as carbazoles and formic acid, its impact on piperidine dehydrogenation remains unexplored [27–29]. In addition, the optimal reaction substrates and mechanism for bio-based piperidine dehydrogenation have yet to be clearly defined. Therefore, this work aims to investigate the size effect of Pd species and establish the optimal LOHC system for bio-based piperidine.

In this report, we presented a bio-based LOHC system based on the piperidine/pyridine, employing size-controlled Pd/C catalysts to establish critical structure-activity relationships in dehydrogenation. Detailed catalyst characterization revealed the relationship between the particle size of the Pd species and dehydrogenation efficiency. We identified Pd NCs (~1.8 nm) as the optimal active sites for the dehydrogenation reaction by integrating multiple characterization techniques, including transmission electron microscopy (TEM), in situ CO diffuse reflectance infrared Fourier transform (CO-DRIFT) spectroscopy, electrochemical CO stripping, X-ray photoelectron spectroscopy (XPS), and X-ray absorption fine structure (XAFS). The catalytic activity exceeds the previously reported systems by several times. Density functional theory (DFT) calculations have shown how the position of methyl groups affects the energy barriers during the dehydrogenation process, providing deeper insights into the performance of the system. *In situ* Fourier transform infrared (FT-IR) spectroscopy has captured reaction intermediates, further elucidating the underlying reaction pathways. Additionally, the applicability of this LOHC system to deuterium storage was investigated, showing promising results for broader hydrogen isotope applications. The study underscores the scalability, stability, and environmental advantages of bio-based piperidine derivatives as LOHCs, reinforcing their potential as a sustainable hydrogen storage solution.

2. Methods

2.1. Reagents

Palladium acetate ($Pd(OAc)_2$) was obtained from Kunming BOREN Metal Materials Co., and the Vulcan carbon black was obtained from CABOT. Sodium borohydride ($NaBH_4$) was purchased from Tianjin Kemiou Chemical Reagent Co., Ltd., and acetone (≥99.6 %) from Sinopharm Chemical Reagent Co. Ltd. *n*-octane, *n*-dodecane, and all piperidines were provided by Adamas-beta. Pure water was supplied by Wahaha. All reagents were used as received without further purification.

2.2. Preparation of supported Pd catalysts

Catalysts with varying Pd particle sizes were obtained by adjusting the Pd loading and reduction method. In a typical synthesis, 200 mg of carbon-support was dispersed in 20 mL of acetone and sonicated for 30 minutes to create a uniform suspension. A 0.02 mol/L solution of Pd $(OAc)_2$ was then added to the suspension during sonication, followed by an additional 30 minutes of sonication. The mixture was stirred at room temperature for 3 hours. Afterward, the acetone was removed using a rotary evaporator, and 10 mL of pure water was added to form a new suspension. While stirring the suspension in an ice-water bath, 10 mL of a 0.1 mol/L aqueous $NaBH_4$ solution was introduced, and the mixture was stirred for an additional hour. The resulting solids were filtered and thoroughly washed with pure water. Finally, the catalyst was dried under vacuum at room temperature for 24 hours, obtaining the final catalyst, denoted as Pd5/C (where 5 indicates a 5 % Pd loading). Two additional catalysts, labelled Pd5/C_{-150} and Pd5/C_{-300}, were prepared by reduction using 5 % H_2/Ar in a tube furnace at 150°C and 300°C, respectively, instead of $NaBH_4$. The synthesis of Pd_{SA}/C was similar to the others, except that the detergent was replaced by DMSO and pure water, and after drying, the catalysts were calcined at 500°C for 5 h under Ar atmosphere.

2.3. Dehydrogenation/hydrogenation performance tests

Methylpiperidine was used as the substrate for the dehydrogenation reaction, which was conducted in a Schlenk tube. In a glove box, the substrate (e.g., 3-methylpiperidine, 1 mmol), 2 mL of *n*-octane as solvent, and 2.35 mol% of the Pd/C catalyst were added to the tube. Before the reaction, the Schlenk tube was purged with argon gas for 10 minutes to remove any air, allowing the reaction to proceed under near-atmospheric pressure. The reaction was then carried out at 120°C internal temperature. Upon completion, the mixture was cooled to room temperature, and the conversion and yield were analyzed by gas chromatography (GC) using *n*-dodecane as the internal standard. Gaseous products analyzed by Pfeiffer Vacuum PrismaPro® QMG 250 mass spectrometry. The spent catalyst was collected via centrifugation, washed three times with ethanol and purified water, and then dried under vacuum at room temperature for 24 hours. Stability tests were conducted by reusing the spent catalyst for subsequent reaction cycles. For scale-up experiments, a condenser was attached to the Schlenk tube, and the reaction was refluxed in an open system with stirring under a stream of argon for the designated time (Fig. S26).

The hydrogenation reaction was performed in a 20 mL batch reactor. In a glove box, the substrate (e.g., 3-methylpyridine, 1 mmol), 2 mL of *n*-octane as solvent, and 50 mg of the Pd/5 C catalyst were added to the reactor. Prior to the catalytic test, the reactor was flushed with 0.5 MPa

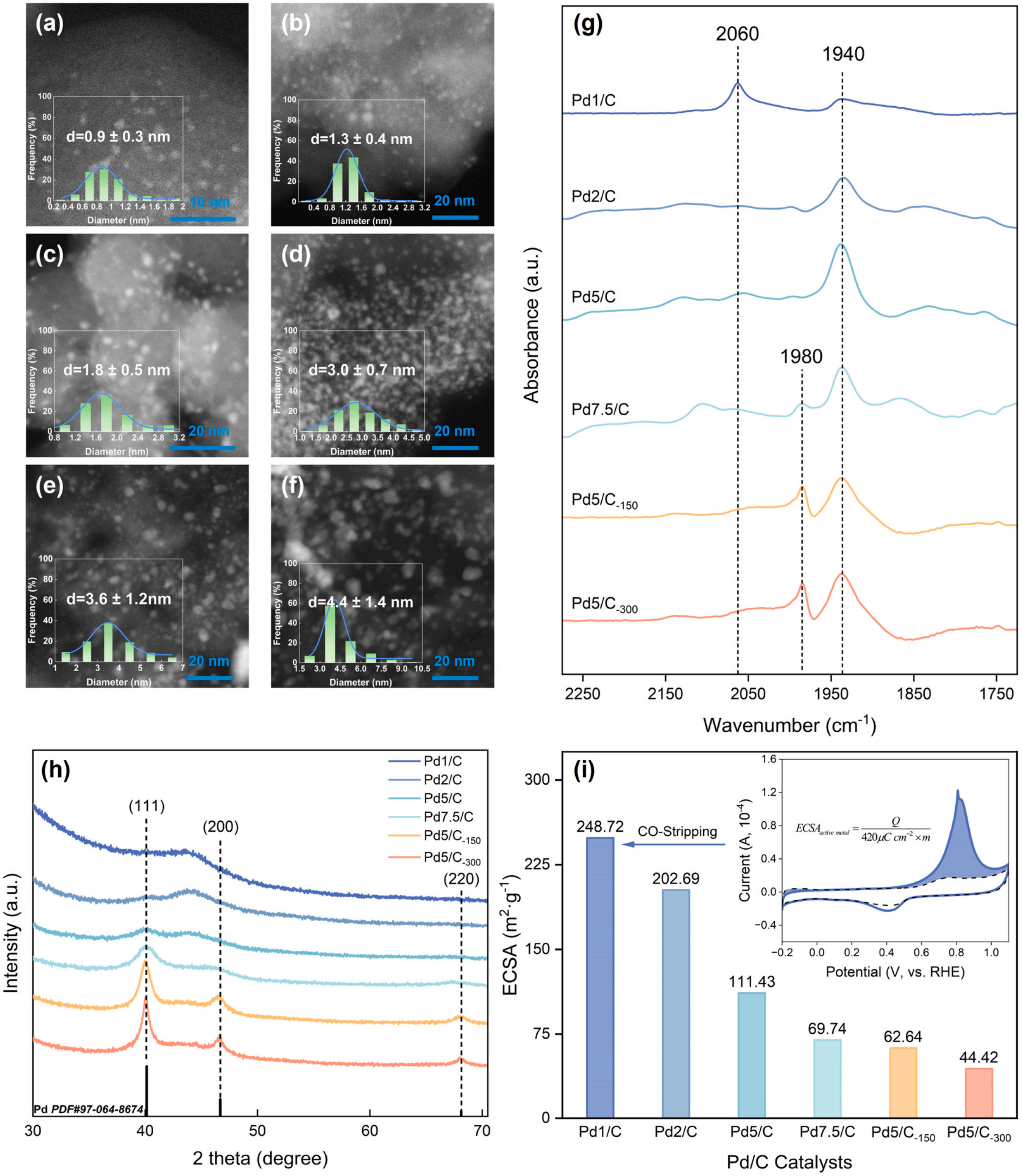

Fig. 1. Morphology properties of different Pd/C catalysts. (a-f) HAADF-STEM image of (a) Pd1/C, (b) Pd2/C, (c) Pd5/C, (d) Pd7.5/C, (e) Pd5/C$_{-150}$, and (f) Pd5/C$_{-300}$, respectively. (g) CO-probe DRIFT spectra of different Pd/C catalysts. (h) XRD of Pd/C catalysts. (i) ECSA of Pd/C catalysts tested by electrochemical CO-stripping.

of hydrogen gas for five cycles, then pressurized to a total pressure of 1 MPa with H_2. The reaction proceeded at 150°C after sealing the reactor. After cooling to room temperature, the conversion and yield were again determined by GC, using *n*-dodecane as the internal standard.

2.4. Materials characterization

High-angle annular dark-field scanning transmission electron microscopy (HAADF-STEM), high-resolution transmission electron microscopy (HRTEM), and corresponding elemental mapping images were collected by field emission high resolution transmission electron mi-

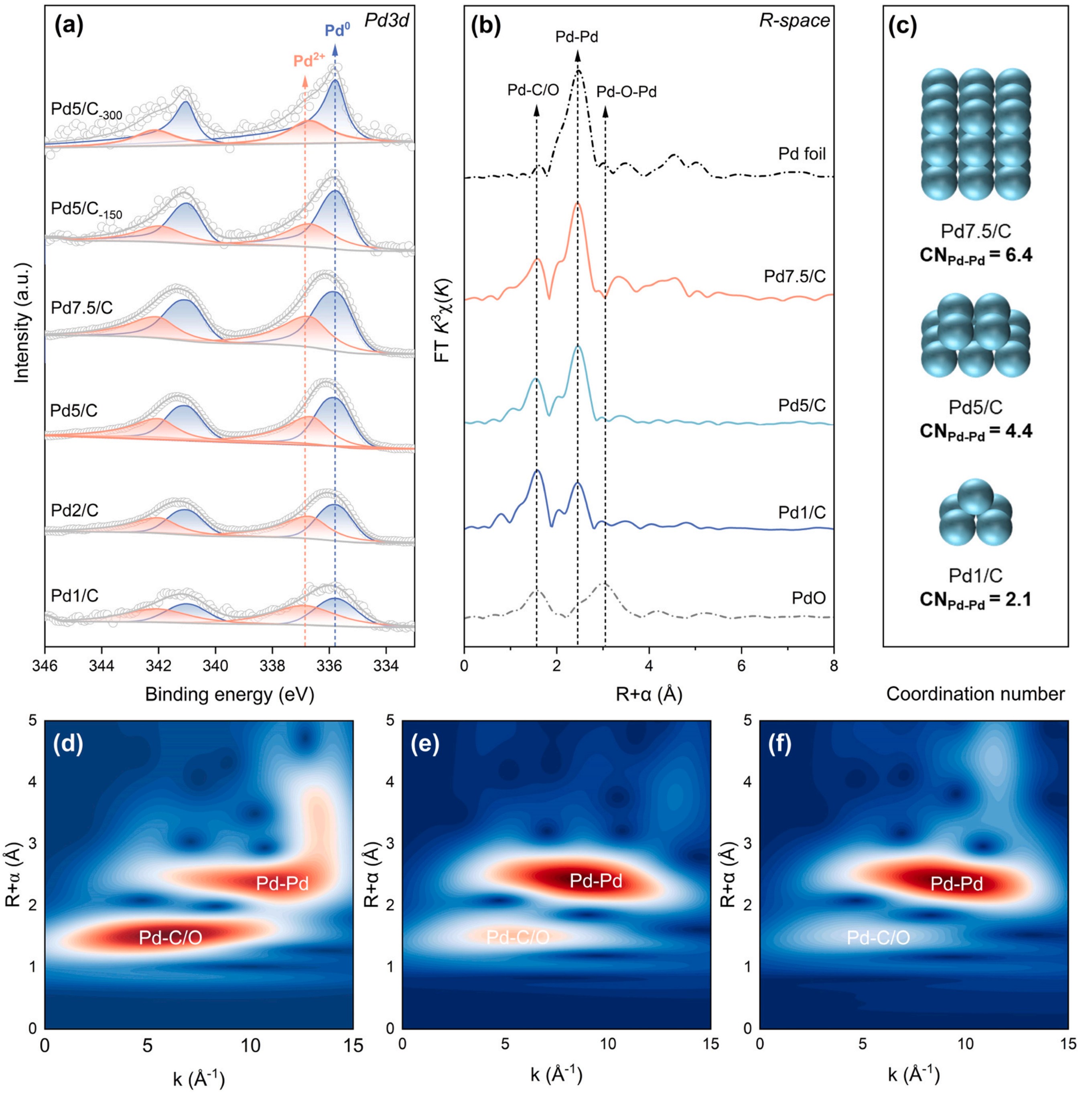

Fig. 2. Electronic structure and coordination of different Pd/C catalysts. (a) Pd 3d core-level XPS spectra. (b) FT-EXAFS spectra in R space. (c) $CN_{Pd\text{-}Pd}$ at different particle sizes and (d-e) Wavelet transformation for the Pd *K*-edge EXAFS signals of (d) Pd1/C, (e) Pd5/C, and (f) Pd7.5/C.

croscopy (JEOL, JEM-F200, Japan) at 200 kV. The particle size distributions and the average particle sizes of Pd were calculated by counting more than 100 particles in the TEM images. XPS was performed on an Axis Supra+ (Shimadzu Company, JAPAN) with a vacuum sample disk. An X-ray photoelectron spectrometer operated at a pressure of $2\cdot10^{-9}$ Pa using monochromatized Al Kα radiation (1486.6 eV) energy scans range from 1100 to −10 eV. All binding energies were calibrated by C1s peak of adventitious carbon (284.8 eV). The nitrogen adsorption-desorption isotherms were measured at 77 K using Micromeritics ASAP 2460. All samples were pretreated at 120 °C for 4 h while maintaining a vacuum condition to remove moisture and impurities. Then, the specific surface area was calculated by applying the Brunauer-Emmett-Teller (BET) method. Additionally, the signals for H_2 ($m/z = 2$) and D_2 ($m/z = 4$) were monitored by Pfeiffer Vacuum PrismaPro® QMG 250 mass spectrometry. The Pd content of the catalysts was determined by ICP-MS using a Shimadzu 2030. The catalysts were pretreated in aqua regia, which is a 3:1 volumetric mixture of HCl and HNO_3 at 95 °C for 4 h, to completely dissolve Pd. The solution was filtered by a syringe filter, diluted in the detectable range, and then analysed. The crystalline phase and the relative crystallite size of the catalysts were analysed by X-ray diffraction (XRD) patterns, which were operated through Bruker D8 ADVANCE machine at 40 kV and 40 mA. The samples were finely ground before analysis, and measured in the scan range from 10 to 90°. The scan speed and scanning step size were $1.0^\circ\cdot\min^{-1}$ and 0.2°, respectively, to record XRD patterns with high resolution. *In situ* FT-IR spectroscopy and CO-DRIFT spectroscopy were performed on a Nicolet iS50 FTIR spectrometer with 32 scans at 4 cm^{-1} resolution. Pd *K*-edge X-ray absorption spectra (XAS) were collected in transmission mode at the Shanghai Synchrotron Radiation Facility (SSRF). Electrochemical active surface area (ECSA) was measured by electrochemical CO-stripping. CO was first bubbled into a saturated 0.1 M H_2SO_4 solution for 15 min, and then N_2 was bubbled for 15 min during a 0.2 V hold to remove dissolved CO. Finally, CO stripping was performed in the potential range of −0.2–1.1 V at a scan rate of 10 mV/S. The area of CO oxidation peak in the first cycle (that is, the area of the CO oxidation peak obtained by subtracting the second cycle from the first cycle) is used to integrate the charge number and then divided by 420 uC/cm^2 to obtain the area, which is then divided by the mass of Pd on the electrode to obtain the ECSA.

$$ECSA_{activemetal} = \frac{Q}{420\mu C{\cdot}cm^{-2} \times m}$$

Q: the charge number; m: the mass of Pd on the electrode; the charge density for the oxidation of the CO monolayer is 420 μC/cm^2.

2.5. DFT calculation

All the DFT calculations were performed using the Vienna ab-initio simulation package (VASP). The projector-augmented wave (PAW) method was used to represent the core-valence interaction [30,31]. The plane wave energy cutoff was set to 450 eV. The generalized gradient approximation (GGA) with the Perdew-Burke-Ernzerhof (PBE) exchange-correlation functional were used in our calculations [32]. The Brillouin zone was sampled at Gamma point with the 3 × 3 × 1 k-point meshes for Pd (111) surface. The energy and force criterion for convergence of the electron density are set at 10^{-5} eV and 0.05 eV/Å, respectively.

3. Results and discussion

3.1. Morphology and electronic structure characterization

A series of carbon-supported Pd catalysts with controlled particle sizes were synthesized through systematic adjustments of Pd loading and preparation protocols. The morphological evolution of Pd/C catalysts was investigated by TEM (Figs. 1a - 1f and Fig. S1). At low Pd loading (0.25 wt%), the Pd species were atomically dispersed on the carbon-support (Fig. S1), while when the loading was increased to 1–2 wt%, Pd species exhibited uniform dispersion with mean diameters of 0.9 nm and 1.3 nm, respectively (Figs. 1a, 1b). Remarkably, the Pd5/C catalyst maintained sub-2 nm particles (~1.8 nm) despite increased metal loading (5 wt%, Fig. 1c). Energy-dispersive X-ray spectroscopy (EDS) elemental mapping verified the uniform distribution of Pd species on the carbon-support (Fig. S2). HRTEM analysis revealed distinct lattice fringes with a spacing of 0.225 nm, corresponding to the Pd (111) crystallographic plane (Fig. S3). A critical threshold emerged at 7.5 wt% Pd loading, where particle size abruptly increased to 3.0 ± 0.7 nm (Fig. 1d). Figs. 1e and 1f display the STEM images of Pd5/C reduced with hydrogen at 150°C and 300°C, respectively. Under hydrogen reduction conditions, a notable increase in Pd particle size was observed, correlating with the rise in reduction temperature, and the extent of agglomeration intensified.

In situ CO-DRIFT spectroscopy was utilized to investigate the structural evolution of active sites in Pd/C catalysts (Fig. 1g). Three characteristic peaks were observed in the range of 1800–2200 cm^{-1}, corresponding to CO adsorption on different Pd nanostructures. Pd1/C manifested two CO-adsorption peaks at 2060 cm^{-1} and 1940 cm^{-1}. The dominant peak (2060 cm^{-1}) was attributed to the linearly bonded CO on atomically dispersed Pd species or at the edges of the Pd sub-NCs (<1 nm), while the 1940 cm^{-1} peak was observed in all Pd/C catalysts. In particular, the Pd2/C and Pd5/C samples exhibited only the 1940 cm^{-1} peak. Combined with TEM results, we infer that the 1940 cm^{-1} peak is attributable to bridge-bonded CO at the edges of Pd NCs (1–2 nm). Notably, the intensity of this peak was significantly higher in Pd5/C compared to Pd2/C, indicating an increased density of bridged adsorption sites per unit mass of Pd NCs, which is consistent with TEM observations. Moreover, the disappearance of the 2060 cm^{-1} peak marks the transition from sub-NCs to NCs, resulting in the replacement of isolated sites by surface-continuous sites. With a further increase in average particle size, we observed a gradual enhancement of the signal at 1980 cm^{-1}, which is derived from bridge-bonded or triple-bonded CO on Pd NPs (>2 nm) or multi-particle ensembles. Concurrently, the weakening of the 1940 cm^{-1} peak suggests a decrease in the number of multifaceted terrace sites and metal-support interfacial sites.

The XRD spectra (Fig. 1h) show characteristic peaks of metallic Pd at 40.12°, 46.67°, and 68.13°. The signal intensity of these peaks correlates with the variation in Pd particle size. Notably, the strongest peak at 40.12° corresponds to the Pd (111) crystal plane, aligning with the HRTEM results. The ECSA of the catalysts was measured by electrochemical CO-stripping. As shown in Fig. 1i and Fig. S4, Pd1/C exhibited the highest ECSA value (248.72 m^2/g, Pd). With increasing Pd loading, the ECSA value decreased rapidly from 202.96 to 44.42 m^2/g. which aligned with the increasing intensity of the Pd (111) diffraction peak in the XRD data (Fig. 1h). Inductively coupled plasma mass spectrometry (ICP-MS) confirmed that the Pd content in all Pd/C samples matched the expected values (Table S1). Additionally, the specific surface areas of carbon-support and Pd/C catalysts, estimated using the BET method, showed a marked reduction in N_2 adsorption and surface area upon Pd loading (Table S1). The decrease in surface area became more pronounced with higher Pd loading. Combined with the TEM analysis, this suggests that the smaller Pd species were uniformly dispersed on the support surface and block some of the smaller pore structures [33].

The electronic structure of the Pd/C catalysts in the Pd 3d region were analysed using XPS. As depicted in Fig. 2a, the binding energy for Pd^0 within the Pd $3d_{5/2}$ region is centred at 335.8 eV, while the binding energy for Pd^{2+} appears between 336.6 and 336.9 eV. The results reveal that as the particle size increases, the relative intensity of the Pd^0 peak also increases, whereas the intensity of the Pd^{2+} peak decreases. Additionally, the Pd 3d peak shifts to lower binding energy as Pd dispersion decreases; it is noteworthy that the peak of Pd^{2+} moves to a lower binding energy with the increase of particle size (336.9–336.6 eV). Based on previous studies, we infer that the Pd^{2+} species in the catalysts arise from unstable Pd near the particle surface. As particle size increases, the amount of surface-exposed unstable Pd also rises, and its reaction with oxygen tends to lower the binding energy of the oxidation state [28,34,35].

The Pd-Pd coordination of catalysts with different particle sizes were determined from Fourier transform extended X-ray absorption fine structure (FT-EXAFS) analysis (Fig. 2b) [36,37]. From Pd1/C to Pd7.5/C, the intensity of the Pd-Pd peak at 2.5 Å gradually increases, while the intensity of the Pd-C/O peak at 1.6 Å slightly decreases. This trend reflects the structural evolution of Pd species from sub-NCs composed of only a few atoms to the formation of larger Pd NPs. This structural evolution is more clearly shown by the wavelet transformation of Pd *K*-edge EXAFS signals (Fig. 2d-f). The absence of the Pd-O-Pd (3.1 Å) peak, on the other hand, indicates that only a small amount of Pd in the surface layer of the Pd NPs is oxidized, without forming agglomeration of Pd NPs. Additionally, the Coordination number of Pd ($CN_{Pd\text{-}Pd}$) increases monotonically with Pd particle size, from 2.1 for Pd1/C to 4.4 for Pd5/C and 6.4 for Pd7.5/C.

3.2. The catalytic performance for dehydrogenation reaction

The results indicate that Pd species in the Pd/C catalyst exhibit large-gap morphology, providing an effective platform for investigating size-dependence in the methylpiperidine dehydrogenation reaction. We evaluated the reactivity of various Pd/C catalysts for the dehydrogenation of 3-methylpiperidine at 120°C and atmospheric pressure. Pristine

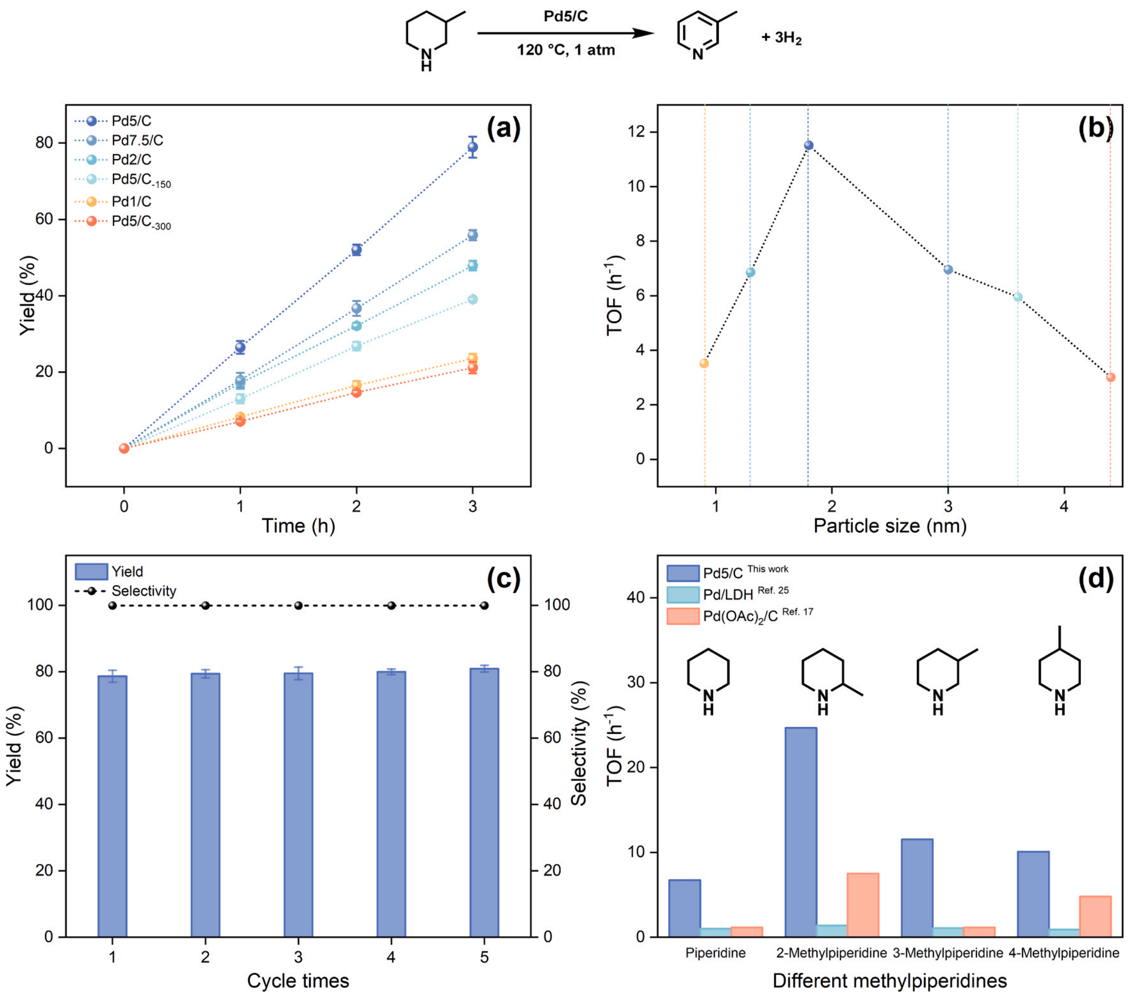

Fig. 3. Dehydrogenation performance of 3-methylpiperidine over different Pd catalysts. (a) Time-dependent activity of different catalysts in the dehydrogenation reaction of 3-methylpiperidine. (b) Different Pd particle sizes as a function of TOF in the dehydrogenation reaction of 3-methylpiperidine. (c) Cyclic stability testing of Pd5/C in the dehydrogenation of 3-methylpiperidine. (d) Performance of Pd catalysts in terms of TOF for dehydrogenation piperidine and 2-/3-/4-methylpiperidines. (The default reaction conditions for a typical dehydrogenation reaction were as follows: temperature (T) = 120 °C, reaction time (t) = 3 h, substrate = 1 mmol, reaction atmosphere: Argon, and catalysts amount: 2.35 mol%.).

C without Pd loading (Fig. S13) and Pd_{SA}/C (Fig. S14) did not catalyse the reaction. Analysis of the gaseous products using a mass spectrometer confirmed the production of high-purity hydrogen (Fig. S15). As shown in Fig. 3a, significant variations in catalytic performance were observed across the catalysts. Pd5/C exhibited the highest catalytic activity over reaction times of 1–3 hours. Although Pd5/C, Pd5/C_{-150}, and Pd5/C-$_{300}$ shared the same Pd loadings, differences in particle size resulted in varying catalytic performances, underscoring the size-dependence of piperidine dehydrogenation activity. Interestingly, despite its smaller particle size and higher ECSA, the Pd1/C catalyst was less active than Pd5/C. This suggests that the presence of multiple neighbouring Pd atoms enhances the efficiency of 3-methylpiperidine dehydrogenation.

We established a critical structure-activity relationships between the particle size of Pd species and hydrogen release performance. The activity followed a volcano-shaped trend (Fig. 3b), with Pd5/C showed the highest activity among the Pd/C catalysts, achieving a 50–280 % increase in turnover frequency (TOF). Combining the findings from morphology and electronic structure characterization, the Pd NCs represent the most active structures, with activity improving as NCs grow the number of neighbouring active sites increases (1.2–1.8 nm). In contrast, although Pd1/C exhibits a larger ECSA, its catalytic activity is lower due to the limited number of effective active sites. When Pd loading was further increased or more severe reduction conditions were applied, metal agglomeration occurred, reducing the number of exposed active sites and decreasing catalytic activity. This explains the diminished activity of Pd species larger than 2 nm. To exclude the influence of residual B element from $NaBH_4$ reduction, we compared the activity of two catalysts with similar sizes but different treatments (Fig. S16). Cycle stability tests were conducted on the Pd5/C catalyst (Fig. 3c). The catalyst remained active without degradation, and no by-products were produced after five reaction cycles. TEM analysis of the used Pd5/C catalyst (Fig. S17) indicated that the particle size remained stable at ~1.8 nm, with no signs of agglomeration or sintering. These results suggest that the catalyst possesses excellent reusability.

To identify the most effective piperidine-based compounds for biomass-derived LOHC applications, we investigated bio-based piperidine derivatives with different methyl group positions. Our results revealed that methyl group positioning significantly influences dehydrogenation activity (Fig. 3d). For unsubstituted piperidine, despite its high theoretical HSC, the dehydrogenation yield was only 47 %, with a TOF of 6.73 h^{-1}. Introducing a methyl group substantially increased the dehydrogenation efficiency, with TOF of 10.08 h^{-1} and 11.52 h^{-1} observed for 4-methyl and 3-methyl isomers, respectively. Notably, when the methyl group was positioned adjacent to the nitrogen atom, as in 2-methylpiperidine, the dehydrogenation efficiency reached a remarkable TOF of 24.67 h^{-1}. Beyond these findings, we compared the catalytic performance of our Pd5/C catalyst with previously reported systems. The results demonstrated that Pd5/C outperforms these

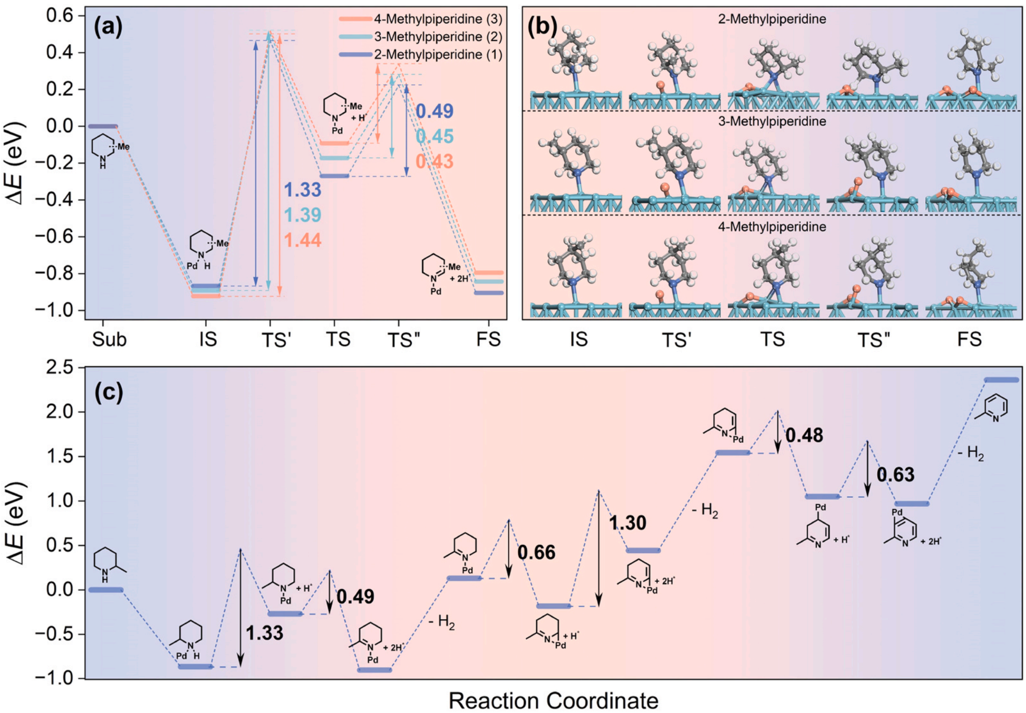

Fig. 4. Pd catalysed DFT calculations of 2-/3-/4-methylpiperidine. (a) Reaction pathways and energy barriers for initial-stage dehydrogenation of 2-/3-/4-methylpiperidines on the Pd (111). (b) Corresponding initial state (IS), transition state (TS) and final state (FS) configurations. (c) 2-Methylpiperidine full dehydrogenation pathway simulations. Pd, dark cyan; H (non-activated), white; H (activated), yellow; C, grey; and N, blue.

systems, achieving significantly higher dehydrogenation activity[17, 25]. The Pd5/C catalyst proved to be equally effective for the dehydrogenation of 2-methyl and 3-methylpiperidines under scaled-up conditions (Scheme S1). Specifically, for 3-methylpiperidine, a catalyst dosage of 100 mg yielded a turnover number (TON) of 1060 after an extended reaction period. In the case of 2-methylpiperidine, the TON reached 2083, further underscoring the high activity and stability of Pd5/C. Notably, under scaled-up conditions, the activity was significantly higher under solvent-free conditions compared to solvent-containing conditions (Fig. S18). This suggests that eliminating the solvent can substantially improve reaction efficiency, especially in large-scale applications.

3.3. *Mechanistic investigations*

To analyse the dehydrogenation conformational relationships of methylpiperidine derivatives, we systematically investigated the dehydrogenation pathways of 2-/3-/4-methylpiperidines in the Pd (111) plane using DFT calculations (Fig. 4). The results reveal that the position of the methyl substituent significantly influences the activation energy barrier for the first N-H bond cleavage. 2-Methylpiperidine (neighbouring substitution) exhibits the lowest energy barrier (1.33 eV), which is 4.3 % and 7.6 % lower than that of the 3-methyl (1.39 eV) and 4-methyl (1.44 eV) isomers, respectively (Fig. 4b). This trend aligns with the experimental activity data, suggesting that the adjacent methyl group enhances the activation of the N-H bond and thus facilitates the initial dehydrogenation step.

Full dehydrogenation pathway simulations further showed that the second dehydrogenation step of 2-methylpiperidine has an energy barrier of 1.96 eV (Fig. 4c), which constitutes the reaction decisive step. This energy barrier distribution feature leads to a significant thermodynamic driving force between the intermediate semi-dehydrogenation state ($\Delta E = 1.96$ eV) and the fully dehydrogenated state ($\Delta E = 1.11$ eV), which drives the reaction towards the fully dehydrogenated product rather than staying in the intermediate stat. The high agreement between theoretical calculations and experimental kinetic data confirmed the key role of methyl position in regulating the dehydrogenation pathway of LOHC and provides an atomic scale basis for the rational design of bio-based hydrogen storage molecules.

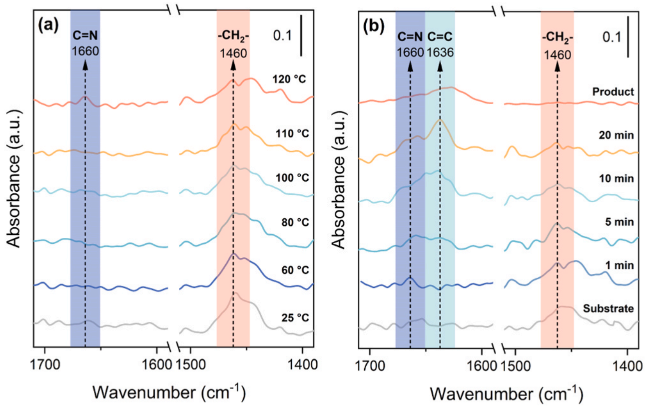

Fig. 5. *In situ* FT-IR of the Pd5/C catalyst during the dehydrogenation of 3-methylpiperidine. (a) the warming process (25°C - 120°C). (b) at 120°C for 1, 5, 10, and 20 min.

To better understand the dehydrogenation mechanism of methylpiperidine over the Pd5/C catalyst, *in situ* FT-IR spectroscopy was employed to capture intermediate products and elucidate reaction pathways. As the reaction temperature increased (Fig. 5a), a characteristic peak at 1460 cm^{-1}, corresponding to the C-H bending vibrations in the methylene (-CH_2-) group of the piperidine ring, diminished significantly above 110°C [38–41]. This indicates the progressive consumption of the substrate. At 120°C, a new characteristic peak appeared at 1660 cm^{-1}, which we attributed to the C=N bond in the double bond region, formed through dehydrogenation at the C-N bond of the piperidine ring [42,43]. As dehydrogenation progressed (Fig. 5b), another

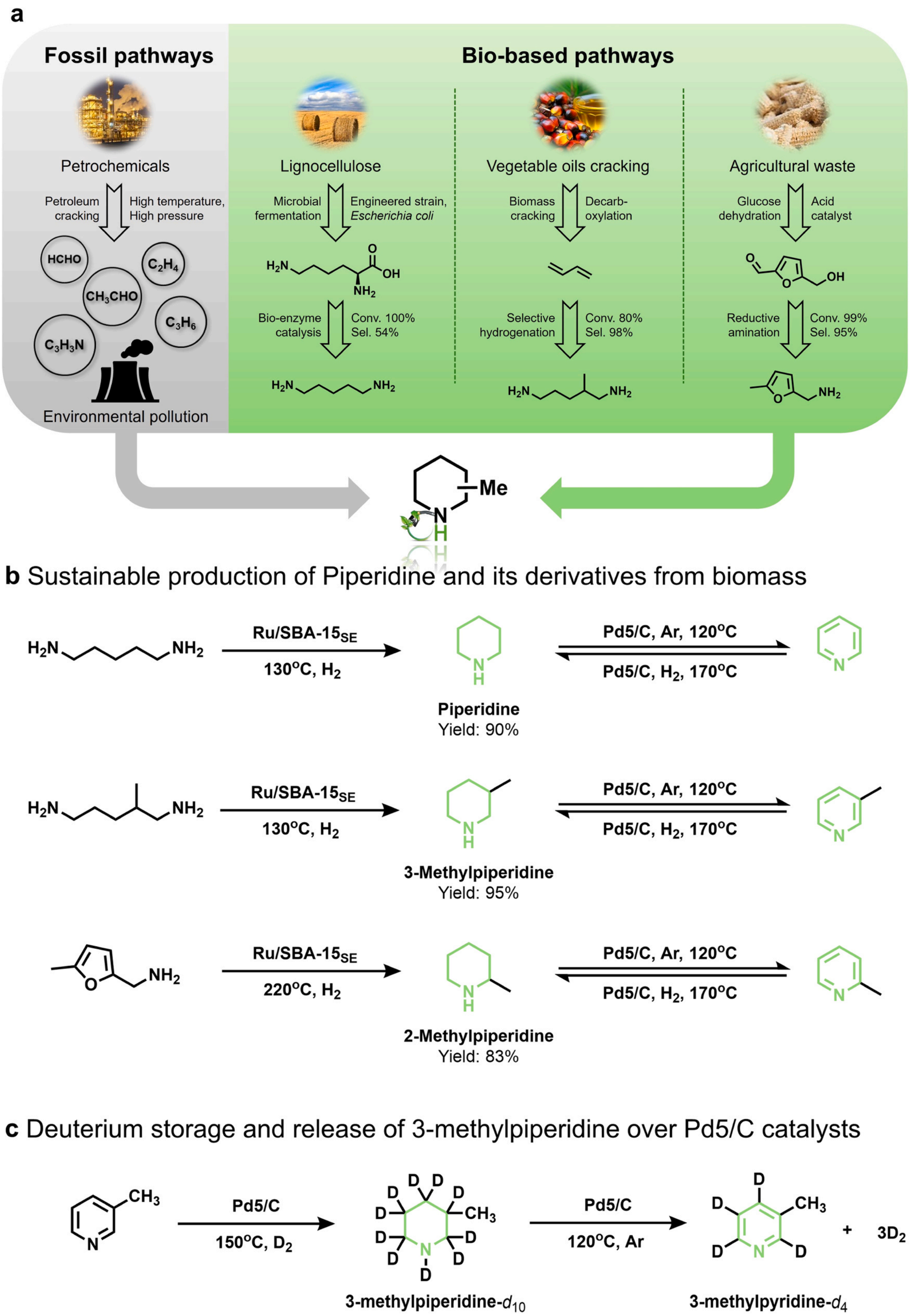

Fig. 6. The synthesis and application of bio-based piperidines in this work. (a) Fossil and bio-based piperidine synthesis pathways. (b) Piperidine derivatives were prepared from biomass feedstock and used as LOHC in this study. (c) Application of bio-based piperidines in deuterium storage and release. (The default reaction conditions for a typical dehydrogenation reaction were as follows: temperature (T) = 120 °C, reaction time (t) = 3 h, substrate = 1 mmol, reaction atmosphere: Argon, and catalysts amount: 2.35 mol%. The default reaction conditions for a typical hydrogenation reaction were as follows: temperature (T) = 170 °C, reaction time (t) = 6 h, substrate = 1 mmol, hydrogen pressure (P) = 1 MPa, and catalysts amount: 50 mg Pd5/C.).

peak emerged at 1636 cm^{-1}, and its intensity eventually surpassed that of the C═N (1660 cm^{-1}). We attributed the 1636 cm^{-1} peak to the C═C bonds formed through dehydrogenation at the C-C bonds in the piperidine ring [44,45]. This signal intensity is consistent with the structural features of the pyridine ring. These findings confirmed that the dehydrogenation process begins with hydrogen removal from the C-N structure, followed by dehydrogenation at the C-C structure. This stepwise sequence provides valuable insights into the dehydrogenation mechanism of the piperidine ring.

3.4. *Bio-based piperidine sources and extend applications*

We then demonstrated a bio-based synthetic route for piperidine derivatives, emphasizing an efficient and sustainable approach to LOHC production (Fig. 6a). Using our recently reported ruthenium (Ru)-based catalyst, piperidine-based compounds can easily prepared from biomass-derived substrates (Fig. 6b) [46]. Piperidine was synthesized via the cyclization of pentanediamine, derived from lignocellulosic lysine, achieving a high yield of 90 % [47–49]. Similarly, 2-methylpiperidine was obtained from 5-methylfurfurylamine—produced from glucose sourced from agricultural waste through acid treatment, dehydration, and reductive amination—with an 83 % yield[22,24,50]. Additionally, we reported the production of 3-methylpiperidine from 2-methylpentanediamine, which can be obtained via the hydrocyanation of butadiene, a byproduct of vegetable oil cracking, achieving a yield of 95 % [46,51,52]. And with significant progress has been made in bio-based butadiene technology, these biomass-derived piperidines highlight their potential as sustainable feedstocks for low-oxygen combustion hydrogen applications, offering an environmentally friendly alternative to traditional synthetic routes.

The Pd5/C catalyst demonstrates remarkable bidirectional functionality in N-heterocyclic LOHC systems (Fig. 6b). Under mild hydrogenation conditions, it achieves near-quantitative conversion of pyridine derivatives to the corresponding piperidines, with yields of 91 % for piperidine and 99 % for both 2-methyl and 3-methylpiperidines, establishing a unified catalytic platform for reversible hydrogen storage/release. Moreover, consistent with dehydrogenation, the methyl group position significantly influenced the hydrogenation efficiency of piperidines, with 2-methylpiperidine exhibiting the highest hydrogenation rate (Fig. S19). Notably, this system exhibits exceptional deuterium storage capabilities. In D_2 atmosphere at 150°C, full deuteration of 3-methylpiperidine to-d_{10} species occurs via sequential D_2 activation and H-D exchange (Fig. S22). A temperature-dependent pathway modulation is observed. At 75°C, selective H-D exchange dominates without further deuteration, yielding fully deuterated 3-methylpyridine-d_4 (Fig. S23). Mass spectrometry confirmed D_2 as the primary gaseous product during dehydrogenation of deuterated piperidinium-d_{10} (Fig. S24), with a kinetic isotope effect (KIE) of 2.32 (Fig. S25). This finding highlights the catalyst's ability to effectively store and release deuterium from the piperidine ring. The unique capability of Pd5/C to manage deuterium isotopes positions it as a promising system for applications in isotope storage and hydrogen isotope management technologies.

4. Conclusion

By integrating precise catalyst engineering with sustainable molecular design, we established a bio-based piperidine LOHC system using size-controlled Pd/C catalysts to explore the structure-activity relationships. Structural characterization and catalytic performance evaluation identified Pd NCs of approximately 1.8 nm as the most active species for the bio-based piperidine dehydrogenation, exhibiting higher efficiency compared with smaller or larger palladium species. Experimental results and DFT calculations revealed that the position of the methyl substituent significantly influences dehydrogenation kinetics, with 2-methylpiperidine exhibiting the highest dehydrogenation efficiency among the studied substrates. The scalability and stability of the Pd catalysts, along with the renewable synthesis route for piperidine derivatives, were also demonstrated. Moreover, the applicability of this system to D storage further highlights its versatility for broader hydrogen isotope applications. Overall, this work not only establishes key structure-activity relationships in Pd-catalysed piperidine dehydrogenation but also demonstrates the feasibility of bio-based piperidines as a sustainable and promising LOHC platform.

CRediT authorship contribution statement

Zihang Yin: Experimental, Characterization, Writing – original draft. **Sicong Ma:** DFT calculation, Writing – calculation section. **Yanwei Cao:** Conceptualization, Supervision, Writing – review & editing. **Lin Chen:** Investigation. **Zhi-Pan Liu:** Software. **Jing Niu:** Investigation. **Fangxiu Ye:** Investigation. **Shutao Xu:** Investigation. **Long Pan:** Supervision. **Lin He:** Supervision, Funding acquisition.

Declaration of Competing Interest

The authors declare that they have no known competing financial interests or personal relationships that could have appeared to influence the work reported in this paper.

Acknowledgements

The work was supported by National Key Research and Development Program of Ministry of Science and Technology (No. 2022YFA1504602), National Natural Science Foundation of China (U22B20137, 22302214, U24A20494). Major Science and Technology Projects in Gansu Province (22ZD6GA003, 23ZDFA016). Gansu Province Basic Innovation Group (24JRRA043). The numerical calculations in this study were carried out on the ORISE Supercomputer. XAFS was conducted at the Shanghai Synchrotron Radiation Facility (SSRF).

Appendix A. Supporting information

Supplementary data associated with this article can be found in the online version at doi:10.1016/j.apcatb.2025.125504.

Data availability

Data will be made available on request.

References

[1] S.O. Jeje, T. Marazani, J.O. Obiko, M.B. Shongwe, Advancing the hydrogen production economy: a comprehensive review of technologies, sustainability, and future prospects, Int. J. Hydrog. Energy 78 (2024) 642–661.

[2] S.E. Hosseini, M.A. Wahid, Hydrogen production from renewable and sustainable energy resources: promising green energy carrier for clean development, Renew. Sustain. Energy Rev. 57 (2016) 850–866.

[3] N. Ma, W. Zhao, W. Wang, X. Li, H. Zhou, Large scale of green hydrogen storage: opportunities and challenges, Int. J. Hydrog. Energy 50 (2024) 379–396.

[4] Q. Hassan, A.Z. Sameen, H.M. Salman, M. Jaszczur, A.K. Al-Jiboory, Hydrogen energy future: advancements in storage technologies and implications for sustainability, J. Energy Storage 72 (2023) 108404.

[5] Z. Gao, A. Li, X. Liu, M. Peng, S. Yu, M. Wang, Y. Ge, C. Li, T. Wang, Z. Wang, Shielding Pt/γ-Mo2N by inert nano-overlays enables stable H2 production, Nature (2025) 1–7.

[6] M. Peng, Y. Ge, R. Gao, J. Yang, A. Li, Z. Xie, Q. Yu, J. Zhang, H. Asakura, H. Zhang, Thermal catalytic reforming for hydrogen production with zero CO2 emission, Science 387 (2025) 769–775.

[7] U. Eberle, M. Felderhoff, F. Schueth, Chemical and physical solutions for hydrogen storage, Angew. Chem. Int. Ed. 48 (2009) 6608–6630.

[8] X. Zhang, Y. Sun, S. Ju, J. Ye, X. Hu, W. Chen, L. Yao, G. Xia, F. Fang, D. Sun, Solar-driven reversible hydrogen storage, Adv. Mater. 35 (2023) 2206946.

[9] H. Kim, H. Kim, W. Kim, C. Kwon, S.-W. Jin, T. Ha, J.-H. Shim, S. Park, A. Jamal, S. Kim, E.S. Cho, Facile synthesis of nanoporous Mg crystalline structure by organic solvent-based reduction for solid-state hydrogen storage, Nat. Commun. 15 (2024) 10800.

[10] R.-G. Ciocarlan, J. Farrando-Perez, D. Arenas-Esteban, M. Houlleberghs, L. L. Daemen, Y. Cheng, A.J. Ramirez-Cuesta, E. Breynaert, J. Martens, S. Bals, J. Silvestre-Albero, P. Cool, Tuneable mesoporous silica material for hydrogen storage application via nano-confined clathrate hydrate construction, Nat. Commun. 15 (2024) 8697.

[11] M.J. Zhou, Y. Miao, Y. Gu, Y. Xie, Recent advances in reversible liquid organic hydrogen carrier systems: from hydrogen carriers to catalysts, Adv. Mater. (2024) 2311355.

[12] J. Wei, M. Zhu, B. Liu, N. Wang, J. Liu, K. Tomishige, S. Liu, G. Liu, Hydrodeoxygenation of oxygen-containing aromatic plastic wastes to liquid organic hydrogen carriers, Angew. Chem., Int. Ed. 62 (2023) e202310505.

[13] Z. Shao, Y. Li, C. Liu, W. Ai, S.-P. Luo, Q. Liu, Reversible interconversion between methanol-diamine and diamide for hydrogen storage based on manganese catalyzed (de) hydrogenation, Nat. Commun. 11 (2020) 591.

[14] P. Preuster, C. Papp, P. Wasserscheid, Liquid organic hydrogen carriers (LOHCs): toward a hydrogen-free hydrogen economy, Acc. Chem. Res. 50 (2017) 74–85.

[15] W. Xue, H. Liu, B. Zhao, L. Ge, S. Yang, M. Qiu, J. Li, W. Han, X. Chen, Single Rh1Co catalyst enabling reversible hydrogenation and dehydrogenation of N-ethylcarbazole for hydrogen storage, Appl. Catal. B 327 (2023) 122453.

[16] Y. Cao, H. Zheng, G. Zhu, H. Wu, L. He, Ceria supported Ru0-Ru+ clusters as efficient catalyst for arenes hydrogenation, Chin. Chem. Lett. 32 (2021) 770–774.

[17] Y. Xie, D. Milstein, Pd catalyzed, acid accelerated, rechargeable, liquid organic hydrogen carrier system based on methylpyridines/methylpiperidines, ACS Appl. Energy Mater. 2 (2019) 4302–4308.

[18] Q. Li, Z. Sun, Y. Wei, Z. Ma, L. Wang, R. Nie, Acceptorless ambient-temperature dehydrogenation and reversible hydrogenation of N-heterocycles over single-atom Co-N-C catalysts, Appl. Catal. B 351 (2024) 123959.

[19] Z. Yin, Y. Cao, W. Sun, G. Chen, X. Fang, L. He, 3-Methylpyridine: synthesis and Applications, Chem. Asian J. 19 (2024) e202400467.

[20] H. Qi, Y. Li, Z. Zhou, Y. Cao, F. Liu, W. Guan, L. Zhang, X. Liu, L. Li, Y. Su, Synthesis of piperidines and pyridine from furfural over a surface single-atom alloy Ru1CoNP catalyst, Nat. Commun. 14 (2023) 6329.

[21] D. Forberg, T. Schwob, M. Zaheer, M. Friedrich, N. Miyajima, R. Kempe, Single-catalyst high-weight% hydrogen storage in an N-heterocycle synthesized from lignin hydrogenolysis products and ammonia, Nat. Commun. 7 (2016) 13201.

[22] H. Qi, Y. Li, Z. Zhou, Y. Cao, F. Liu, W. Guan, L. Zhang, X. Liu, L. Li, Y. Su, K. Junge, X. Duan, M. Beller, A. Wang, T. Zhang, Synthesis of piperidines and pyridine from furfural over a surface single-atom alloy Ru(1)Co(NP) catalyst, Nat. Commun. 14 (2023) 6329.

[23] Y. Elaouzy, A.El Fadar, Water-energy-carbon-cost nexus in hydrogen production, storage, transportation and utilization, Int. J. Hydrog. Energy 53 (2024) 1190–1209.

[24] M. Pelckmans, T. Renders, S. Van de Vyver, B. Sels, Bio-based amines through sustainable heterogeneous catalysis, Green Chem. 19 (2017) 5303–5331.

[25] T. Oyama, T. Yatabe, X. Jin, N. Mizuno, K. Yamaguchi, Heterogeneously palladium-catalyzed acceptorless dehydrogenative aromatization of cyclic amines, Chem. Lett. 48 (2019) 517–520.

[26] D. Ainembabazi, N. An, J.C. Manayil, K. Wilson, A.F. Lee, A.M. Voutchkova-Kostal, Acceptorless amine dehydrogenation and transamination using Pd-doped hydrotalcites, ACS Catal. 9 (2018) 1055–1065.

[27] C. Dong, Z. Gao, Y. Li, M. Peng, M. Wang, Y. Xu, C. Li, M. Xu, Y. Deng, X. Qin, Fully exposed palladium cluster catalysts enable hydrogen production from nitrogen heterocycles, Nat. Catal. 5 (2022) 485–493.

[28] Y. Kim, D.H. Kim, Understanding the effect of Pd size on formic acid dehydrogenation via size-controlled Pd/C catalysts prepared by NaBH4 treatment, Appl. Catal. B 244 (2019) 684–693.

[29] H. Yu, Y. Wu, S. Chen, Z. Xie, Y. Wu, N. Cheng, X. Yang, W. Lin, L. Xie, X. Li, J. Zheng, Pd-modified LaNi5 nanoparticles for efficient hydrogen storage in a carbazole type liquid organic hydrogen carrier, Appl. Catal. B 317 (2022) 121720.

[30] P.E. Blochl, Projector augmented-wave method, Phys. Rev. B 50 (1994) 17953–17979.

[31] G. Kresse, D. Joubert, From ultrasoft pseudopotentials to the projector augmented-wave method, Phys. Rev. B 59 (1999) 1758.

[32] J.P. Perdew, K. Burke, M. Ernzerhof, Generalized gradient approximation made simple, Phys. Rev. Lett. 77 (1996) 3865.

[33] P.-C. Kang, Y.-S. Ou, G.-L. Li, J.-K. Chang, C.-Y. Wang, Room-temperature hydrogen adsorption via spillover in Pt nanoparticle-decorated UiO-66 nanoparticles: implications for hydrogen storage, ACS Appl. Nano Mater. 4 (2021) 11269–11280.

[34] J. Li, W. Chen, H. Zhao, X. Zheng, L. Wu, H. Pan, J. Zhu, Y. Chen, J. Lu, Size-dependent catalytic activity over carbon-supported palladium nanoparticles in dehydrogenation of formic acid, J. Catal. 352 (2017) 371–381.

[35] W. Zhou, J.Y. Lee, Particle size effects in Pd-catalyzed electrooxidation of formic acid, J. Phys. Chem. C. 112 (2008) 3789–3793.

[36] H. Funke, A. Scheinost, M. Chukalina, Wavelet analysis of extended x-ray absorption fine structure data, Phys. Rev. B Condens. Matter Mater. Phys. 71 (2005) 094110.

[37] H. Funke, M. Chukalina, A.C. Scheinost, A new FEFF-based wavelet for EXAFS data analysis, Synchrotron Radiat. 14 (2007) 426–432.

[38] R.N. Jones, A. Cole, The characterization of methyl and methylene groups in steroids by infrared spectrometry. I. Correlations of bending frequencies with molecular structure1, J. Am. Chem. Soc. 74 (1952) 5648–5661.

[39] K. Yatsimirskii, L. Budarin, A. Shtepanek, A. Telyatnik, V. Smirnov, PMR and IR spectra of a new class of macrocyclic compounds, Theor. Exp. Chem. 12 (1976) 326–328.

[40] D. Sun, F. Yu, L. Li, T. Lin, X. Zhu, Effect of chemical composition and structure of asphalt binders on self-healing, Constr. Build. Mater. 133 (2017) 495–501.

[41] E.S. Al-Abdullah, Y.S. Mary, C.Y. Panicker, N.R. El-Brollosy, A.A. El-Emam, C. Van Alsenoy, A.A. Al-Saadi, Theoretical investigations on the molecular structure, vibrational spectra, HOMO–LUMO analyses and NBO study of 1-[(Cyclopropyl-methoxy) methyl]-5-ethyl-6-(4-methylbenzyl)-1, 2, 3, 4-tetrahydropyrimidine-2, 4-dione, Spectrochim. Acta A Mol. Biomol. Spectrosc. 133 (2014) 639–650.

[42] L. Yadav, L. Yadav, Infrared (IR) spectroscopy, Org. Spectrosc. (2005) 52–106.

[43] L. Clougherty, J. Sousa, G. Wyman, C= N stretching frequency in infrared spectra of aromatic azomethines, J. Org. Chem. 22 (1957) 462–4612.

[44] R.H. Wiley, S.C. Slaymaker, H. Kraus, Dimethylhydrazones of aliphatic, aromatic, and heterocyclic aldehydes and their infrared absorption characteristics, J. Org. Chem. 22 (1957) 204–207.

[45] H. Schmiers, J. Friebel, P. Streubel, R. Hesse, R. Köpsel, Change of chemical bonding of nitrogen of polymeric N-heterocyclic compounds during pyrolysis, Carbon 37 (1999) 1965–1978.

[46] Z. Yin, Y. Cao, J. Zhao, L. Pan, T. Wang, X. Fang, L. He, Confined Ru nanoclusters for the low-temperature cyclization of diamines to piperidines/pyridines, ACS Catal. 15 (2025) 3711–3721.

[47] M. Zhao, D. Shi, X. Lu, H. Zong, B. Zhuge, H. Ji, Ethanol fermentation from non-detoxified lignocellulose hydrolysate by a multi-stress tolerant yeast Candida glycerinogenes mutant, Bioresour. Technol. 273 (2019) 634–640.

[48] Z. Chen, G. Liu, J. Zhang, J. Bao, A preliminary study on L-lysine fermentation from lignocellulose feedstock and techno-economic evaluation, Bioresour. Technol. 271 (2019) 196–201.

[49] C. Jin, J. Bao, Lysine production by dry biorefining of wheat straw and cofermentation of Corynebacterium glutamicum, J. Agric. Food Chem. 69 (2021) 1900–1906.

[50] H. Wu, H. Li, Z. Fang, Hydrothermal amination of biomass to nitrogenous chemicals, Green Chem. 23 (2021) 6675–6697.

[51] P. Zámostný, Z. Bělohlav, J. Šmidrkal, Production of olefins via steam cracking of vegetable oils, Resour., Conserv. Recycl 59 (2012) 47–51.

[52] J. Long, T. Wang, H. Zhong, M. Jiao, B. Morandi, L. He, G.J. Cheng, X. Fang, One-step process for the regiodivergent double hydrocyanation of 1, 3-butadiene, Angew. Chem. (2025) e202422337.